

Synchrotron light source X-ray detection with Low-Gain Avalanche Diodes

**S.M. Mazza¹ G. Saito² Y. Zhao¹ T. Kirkes¹ N. Yoho¹ D. Yerdea¹ N. Nagel¹ J. Ott¹
M. Nizam¹ M. Leite² M. Morales⁴ H. F.-W. Sadrozinski¹ A. Seiden¹ B. Schumm¹
F. McKinney-Martinez¹ G. Giacomini³ W. Chen³**

¹*SCIPP, University of California Santa Cruz, 1156 high street, Santa Cruz (CA), US*

²*Universidade de São Paulo, São Paulo (SP), Brazil*

³*Brookhaven National Laboratory, Upton (NY), U.S.*

⁴*IPEN-CNEN, São Paulo (SP), Brazil*

E-mail: simazza@ucsc.edu

ABSTRACT: The response of Low Gain Avalanche Diodes (LGADs), which are a type of thin silicon detector with internal gain, to X-rays of energies between 6-70 keV was characterized at the SLAC light source (SSRL). The utilized beamline at SSRL was 11-2, with a nominal beam size of 3 cm x 0.5 cm, repetition rate of 500 MHz, and very monochromatic. LGADs of different thicknesses and gain layer configurations were read out using fast amplification boards and digitized with a fast oscilloscope. Standard PiN devices were characterized as well. The devices' energy resolution and time resolution as a function of X-ray energy were measured. The charge collection and multiplication mechanism were simulated using TCAD Sentaurus, and the results were compared with the collected data.

KEYWORDS: fast silicon sensors; charge multiplication; thin tracking sensors; X-rays; time resolution

ARXIV EPRINT: [XXXX.XXXX](#)

1 Introduction

Several groups developing Low Gain Avalanche Detectors (LGADs) for use in particle physics applications (e.g., timing layers for ATLAS and CMS [1, 2]) have recently begun to explore the possibility of their application to other fields of science and technology [3]. LGADs are thin silicon sensors with modest internal gain and exceptional time resolution [4, 5]. They comprise a low-doped region called 'bulk', typically 20-50 μm thick, and a highly doped thin region, a few μm from the electrodes, called 'gain layer'. LGADs have a fast rise time, exceptional time resolution, and short full charge collection time.

The response of LGADs to X-rays of energies 6-70 keV (with a precision of 10^{-4}) was characterized at the Stanford Light source (SSRL) [6] at the beamline 11-2 [7]. SSRL 11-2 has a nominal beam size of 3 cm x 0.5 cm, a repetition rate over 500 MHz, and is exceptionally monochromatic. The tested thin LGADs easily resolved in time the 500 MHz repetition rate of the beam line. The energy and time resolution of the tested LGADs were measured as a function of X-ray energy, device type, and gain. The characterization presented in this paper will be increasingly important since emerging prototypes (such as AC-LGADs, TI-LGADs, DJ-LGADs) can reduce the LGAD granularity to the scale of 50 μm or less, allowing the technology to be reliably used for X-ray detection.

Simulation software was employed to understand the behavior of X-ray interaction with the sensors. GEANT was used to evaluate the interaction rate (both full absorption and Compton scattering) in the active volume of the devices. TCAD Sentaurus was used to understand the charge collection mechanism for X-ray interaction in different areas of the LGAD tested.

Device	Producer	BV	Thickness	Gain layer	Geometry
HPK 3.1	HPK	230V	50 μm	shallow	1.3x1.3 mm
HPK 3.2	HPK	130V	50 μm	deep	1.3x1.3 mm
HPK PiN	HPK	400V	50 μm	no gain	1.3x1.3 mm
HPK 3.1 5x5	HPK	230V	50 μm	shallow	1.3x1.3 mm
BNL 20um	BNL	100V	20 μm	shallow	1.3x1.3 mm
BNL AC-LGAD 1 cm	BNL	250V	50 μm	shallow	0.5x1 cm
BNL AC-LGAD 0.5 cm	BNL	250V	50 μm	shallow	0.5x0.5 cm

Table 1: List of tested HPK and BNL LGADs

2 Devices tested

Four standard single pads DC-LGADs from HPK (Hamamatsu photonics) and BNL (Brookhaven National Laboratories) were tested. Devices tested had 50 μm and 20 μm of active thickness. A complete list of the devices is shown in Tab. 1, and pictures are shown in Fig. 1. A shallow and deep gain layer in the table means a gain layer with peaking doping within 1 μm and over 2 μm from the top surface of the detector, respectively. All devices were tested at several voltages up to slightly less than the breakdown voltage. The gain and time resolution as a function of bias voltage in response to minimum ionizing particles (MIPs) for the four devices tested is shown in Fig. 2.

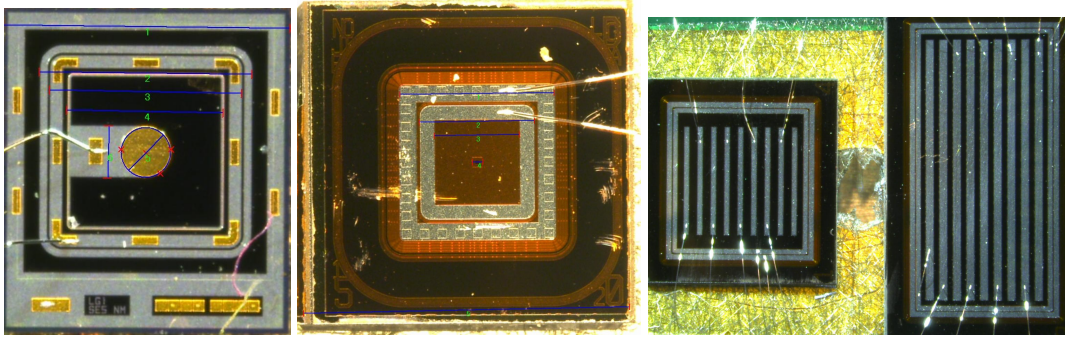


Figure 1: Left: single pad geometry of HPK 3.1, 3.2 LGADs and PiN. Middle: single pad BNL 20 μm LGAD. Right: BNL strip AC-LGADs.

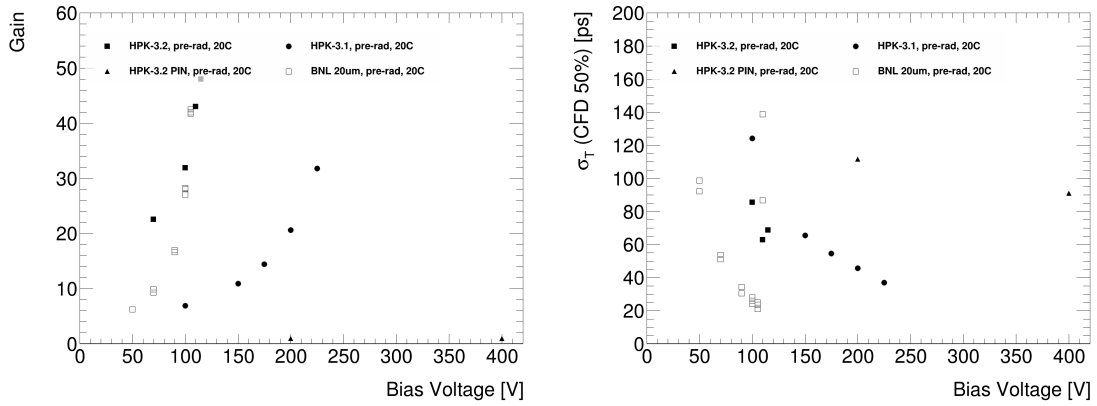


Figure 2: Left: Gain of the devices as a function of bias voltage. Right: Time resolution of the devices as a function of bias voltage. The values were measured with an Sr90 beta source in coincidence with a timing trigger.

3 Experimental setup at SSRL

The experimental setup in the beamline is shown in Fig. 3, Left. The tested LGAD and PiN sensors are mounted on fast analog amplifier boards (bandwidth around 2 GHz), shown in Fig. 3, Right, and digitized by a fast oscilloscope or digitizer. The fast boards have either 1 or 16 channels, and the trans-impedance of the amplifiers is 470 Ω (plus an in-line second-stage amplifier with gain 10) and 5300 Ω , respectively. The oscilloscope used are: 13 GHz bandwidth 128 Gs sample rate keysight oscilloscope, 4 GHz bandwidth 40 Gs LeCroy oscilloscope, CAEN DT5742 16ch digitizer.

The board sits on a 3D-printed stage mounted on X-Y Thorlab motors for fine adjustment. In front of the board, there's an ionization chamber that provides a measurement of the beam intensity. The output of the ionization chamber allows adjusting the monochromator to select the beam's baseline and harmonic (2x the energy) components. The HV and LV are provided by a CAEN tabletop HV power supply and a standard LV power supply, respectively. The components (HV supply, motors, Oscilloscope/digitizer) are remotely controlled from outside the hutch with a laptop that also controls the data taking.

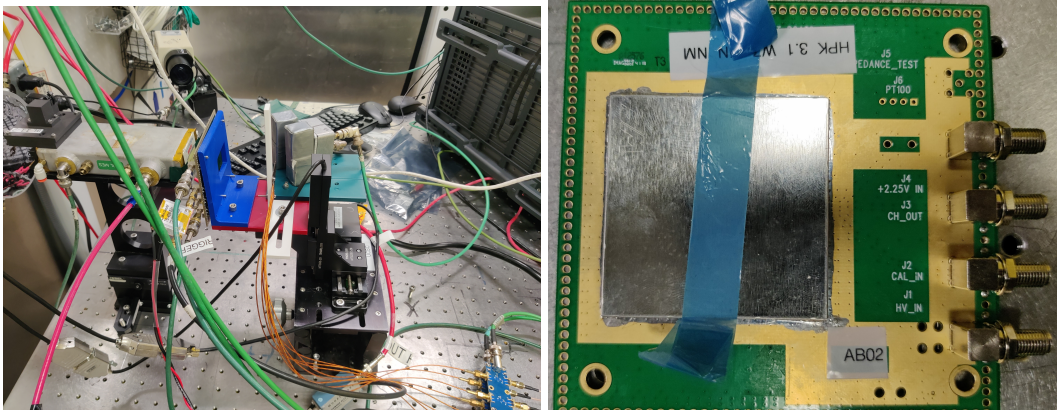


Figure 3: Left: setup at SSRL. Right: single channel board used for sensor testing.

SSRL provides a fast synchronizing signal with the cyclotron with a 1.28 MHz frequency. This signal was used to trigger the data acquisition, allowing each event to have the same bunch structure in time. The beam structure has a window of 100 ns of buckets spaced in time by 2.1 ns separated by 50 ns intervals without buckets except for a single bucket in the center. This beam structure was ideal for device testing since it allows testing the response both for a high repetition rate environment (over 500 MHz) and single buckets.

4 Geant4 simulation

A simulation of the interaction of X-Rays with the test setup was performed using Geant4 Toolkit [8–10]. The simulated structure was comprised of an HPK type 3.2 LGAD sensor attached to a printed circuit board (PCB), acting as a support structure, and the geometry and materials were described in GDML [11]. The Fig. 4 shows all the relevant structures as entered in the simulation. To replicate the test beam conditions, the structure was surrounded by air at room temperature.

The simulation uses the Geant4 standard EM Physics List, and the particles were tracked using production cuts of 100nm and 100eV. All simulations were done for 1M photons. The same beam geometry from the SSRL (flat rectangular beam of 2.5mm x 1.0mm with the center coinciding with the LGAD center) was used in the simulation with fundamental SSRL energies of 5 to 70 keV, in 5 keV steps. The inclusion of energies above the primary beam energy of 37 keV and up to 70 keV takes into account the possibility to adjust the beam line monochromator so that high energy harmonics can be produced, up to 70 keV. No spread in the nominal energy was included in the simulation since the beam energy spread at the SSRL is negligible ($\Delta E/E \approx 10^{-4}$) [7].

4.1 Simulation of the energy deposition

One of the main objectives of the simulation is to understand the energy deposition in the different LGAD structure layers. Differently from the case of high energy physics applications, where a minimum ionizing particle produces ionization charges along its track across the sensor structures, in X-Rays applications the charge will be concentrated at the position where the photon is absorbed, which will in turn depend on the photon energy. The Fig. 5 presents the primary charges distribution for several energies under consideration in this work. Only the charges produced inside the LGAD

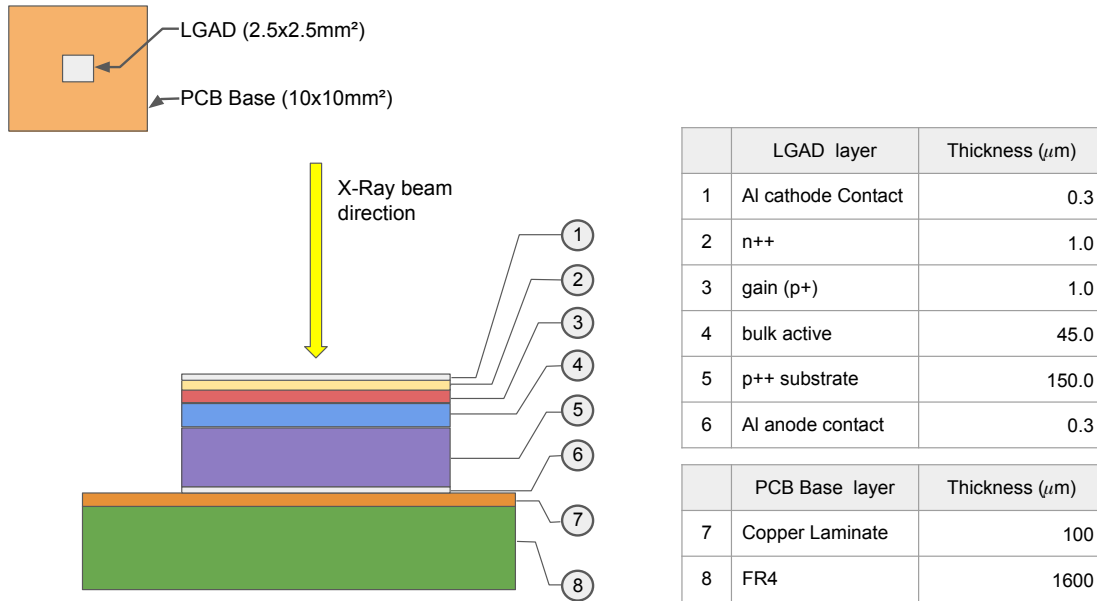


Figure 4: An schematic view of geometry (not in scale) of a HPK type 3.2 LGAD and support structure used in the Geant4 simulation. The direction of the beam is indicated in the figure, as well as the relevant structure cross section dimensions and materials.

volume are accounted (I think this should only be the gain+bulk). The intrinsic energy resolution (calculated as the ratio $\sigma_{N_{\text{primaries}}}/N_{\text{primaries}}$ can be calculated for each distribution and is presented by Fig. 5(b).

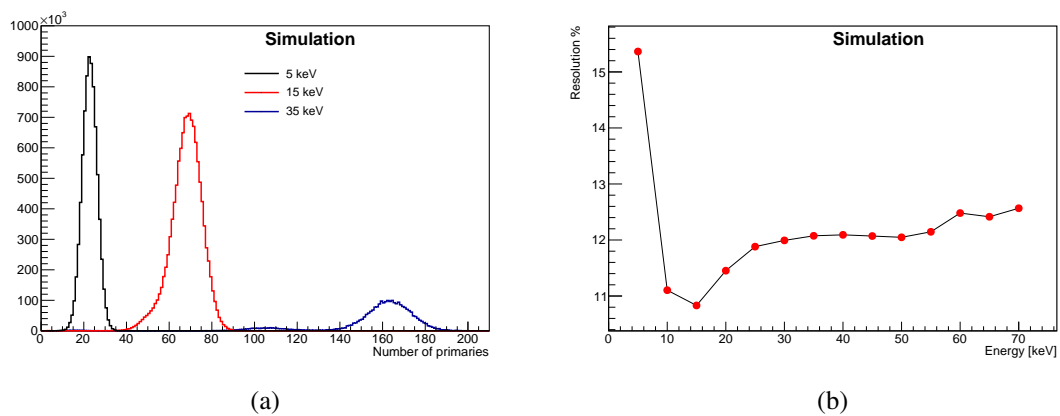


Figure 5: (a) Distribution of the number of primary charges created in the LGAD HPK type 3.2 volume by 5, 15 and 35 keV X-rays photons (10^6 photons in a flat rectangular beam of 2.5mm x 1.0mm); (b) Intrinsic resolution as a function of the X-ray energy.

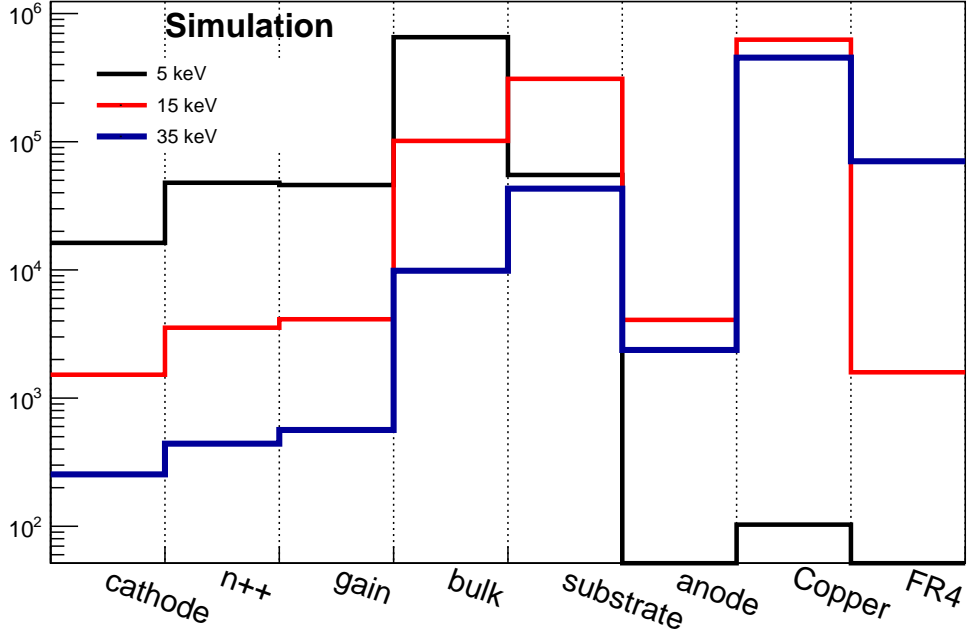


Figure 6: How many times a conversion occurs in each volume of the experimental setup for X-ray energies of 5, 15 and 35 keV (refer to Fig. 4 for a key for each volume number). For each energy a total of 10^6 X-ray photons were shoot perpendicular to the center of the LGAD.

4.2 Simulation of the efficiency and spatial distribution of primaries

Given the low atomic number of the sensor (Silicon) and the micrometric thickness (see Fig. 4) it is important to evaluate the efficiency of detection for X-rays as a function of the energy. To simulate the number of primaries created in each volume, the X-ray beam was changed now to a point-like beam hitting the center of the LGAD structure in perpendicular direction. The Fig. 6 shows how many times a conversion occurs inside a volume of the setup. Again, 10^6 X-ray photons with energies from 5 to 70 keV were simulated, and the results for the energies of 5, 15 and 35 keV are shown in Fig. 6. Only primaries that are created in Volumes 3 and 4 (gain layer and bulk active) will contribute to the signal formation.

The same point-like beam response can be used to evaluate the spatial distribution of the primaries inside the LGAD structure active regions (namely the gain and the bulk active). While this particular device does not have a high segmentation for position-sensitive applications, a very similar structure is used in AC-LGADs hence this type of simulation can provide a handle on the intrinsic spatial resolution that can be obtained with this device (before any effect of charge drift, multiplication and sharing in readout electrodes). The Fig. 7 presents the transverse spatial primaries distribution in the bulk active region for X-rays of 5, 15 and 35 keV.

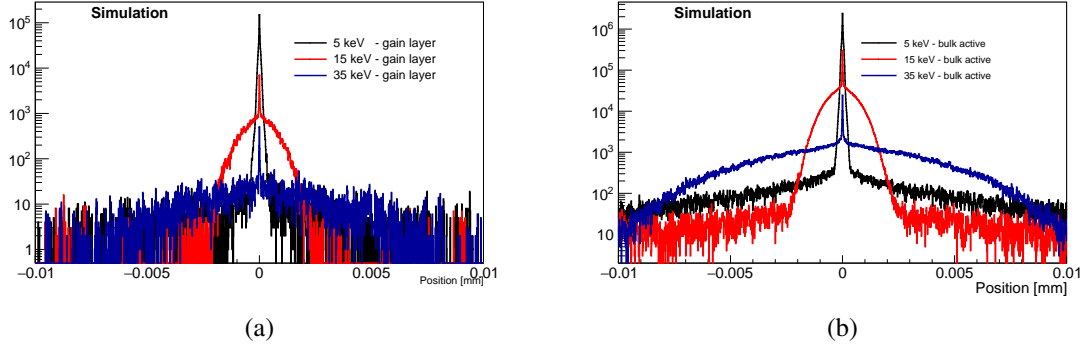


Figure 7: Primary charge transverse distribution (considering a point-like beam) for photons of 5, 15 and 35 keV for LGAD gain layer (a) and bulk active layer (b)

5 TCAD simulation

TCAD software from Synopsys Sentaurus is used to simulate the LGAD response to X-ray photons. In this paper, only photons that are fully absorbed are simulated. The photon absorption is modeled with uniform track with linear energy transfer (LET) that corresponds to the photon energy, and the generated electron-hole pairs are distributed in a $1 \mu\text{m}^2$ box. The simulated current signal at the device level is convoluted with a trans-impedance amplifier (TIA) SPICE model to match the experiment readout setup designed by UCSC-SCIPP, and a software digitization rate of 128-GSample/s is applied to replicate the oscilloscope output.

5.1 Time variation due to different absorption depths

Large time jitter of the signal is observed in the measurement, and a potential explanation for this is related to the depth of the photon absorption. Simulation of single photon absorption with energy of 20 keV at different depths are simulated. The current signals at the device level and convoluted voltage signals are shown in Fig. 8. The time variation on the rising edge is due to the drifting time for generated charges to arrive at the multiplication layer. Multiplication for charge generated at the bottom of the device will have a delay corresponding to the distance of $50 \mu\text{m}$. The maximum time variation among all possible absorption depths is evaluated at different CFD fractions. The time variation increases significantly above CFD 20%, so a low CFD fraction is required to minimize the time variation due to photon absorption depth.

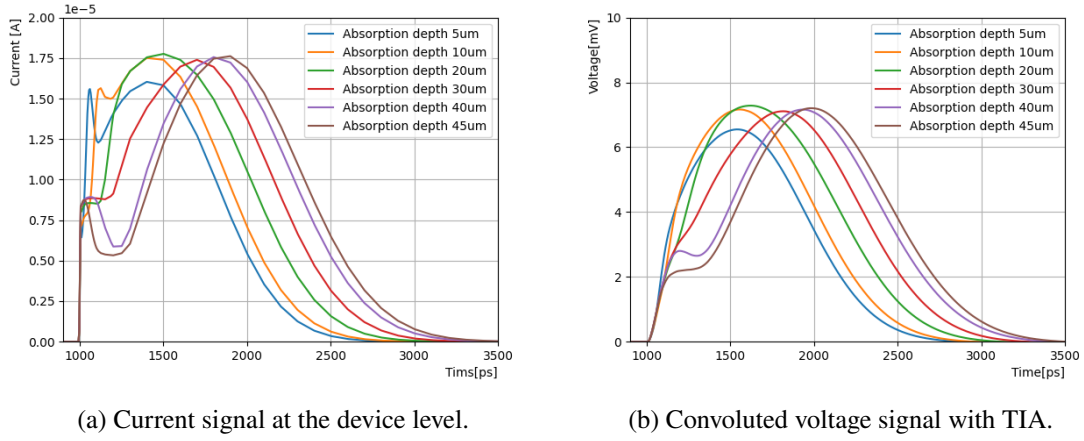


Figure 8: 50um LGAD signal response to a single 20 keV photon at different absorption depth.

5.2 Multiple photons conversion and harmonic energy

Multiple photon conversions within the device can result in the same amount of generated e-h pairs corresponding to the harmonic energy components. For example, the amount of generated e-h pairs corresponds to the total deposited energy of 40 keV can be originated from either two photons conversion with the energy of 20 keV each, or a single photon of 40 keV from the beam harmonics with the energy of 40 keV. In Fig. 9, there's a significant difference in the signal response due to double photon conversion vs single photon from the harmonic. This difference can be explained by the E-field distortion due to the high density of e-h pairs in the gain layer.

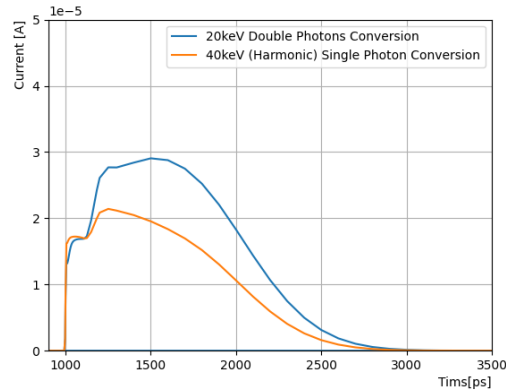


Figure 9: Comparison of generated signal of double photon conversion vs single photon from the harmonic components.

6 Data analysis

The data acquired during the test beam was analyzed using analysis software developed for the project. The code was written in Python 3 using common scientific analysis packages and the

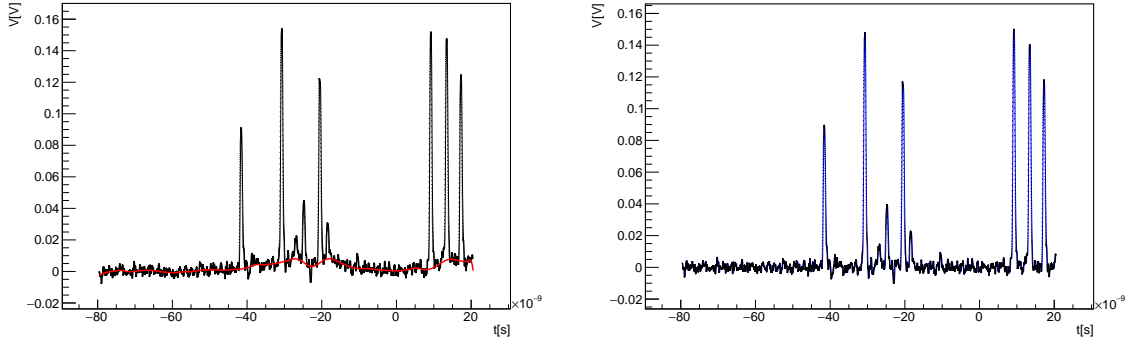


Figure 10: Left: example of a waveform from a HPK Type 3.1 LGAD sensor biased at 200 V exposed to a beam of 35 keV X-rays as acquired by the oscilloscope on the output of the amplifier showing the fluctuation on the voltage baseline level. Right: the same waveform as in the left with the shift on the voltage baseline subtracted.

CERN ROOT environment. The analysis procedure is as follows: first, correct the baseline for each event, then recognize all the peaks in the bunch train and finally analyze the single peaks to get the pulse maximum, area, and time of arrival.

6.1 Baseline Correction

A fluctuation in the baseline level of the signal could be seen in the detected bunch trains, the shift arises from successive X-ray hits on the sensor. In Fig. 10, this fluctuation can be understood as a low-frequency signal added to the response of the sensor to the X-ray hits. Thus being able to find this shift on the baseline of the signal and removing it from the waveform improves the overall estimation of energy and timing resolution of each sensor.

Using an approach from spectroscopy called asymmetrically re-weighted penalized least squares smoothing [12], an efficient baseline fluctuation subtraction was possible. This method uses a very computationally intensive algorithm, being too slow to be applied directly to the fast sampled rate waveforms needing correction. The approach taken was then to first downsample the waveform by an integer factor, lowering the overall amount of samples to be processed. Because of its low-frequency content, the downsampling step can be performed without degrading the information related to the baseline shift. The asymmetrically re-weighted penalized least squares smoothing method was then applied to the downsampled waveform, resulting in a much faster processing time. To be able to subtract it from the original waveform, it was needed to restore the sampling rate of the baseline shift estimation. To upsample the signal, a Fourier-based method is performed followed by a Savitzky-Golay filter with 300 samples and polynomial order of 3 to smooth it. Finally, the baseline shift uncovered by the described method is subtracted from the original waveform as seen in Fig. 10.

6.2 Peak Finding

To evaluate the energy and timing resolution of the sensor, it is needed to extract information for each individual X-ray induced signal. Because all peaks have the same polarity and are induced by

bunches of photons spaced in time by 2.1 ns, a naive approach of finding local maxima separated well separated in time works.

To eliminate noise being interpreted as valid peaks, the standard deviation σ of the first 20 ns, always empty of signals, is calculated and a cut on the amplitude of 7σ of the signal peak is also applied.

6.3 Harmonics component in the beam

The beamline used on the synchrotron is capable of offering an X-ray beam of photons with selected energy with very high energy precision using a monochromator. The beam is also partly contaminated by photons with twice the energy from the harmonic component of the monochromator. These photons with twice that energy are hereafter referred to as harmonics. The harmonic photons can be removed by tuning the monochromator accordingly since they have a much narrower angular distribution.

With a mixed beam, it is possible to identify between the distribution induced by X-rays having the base energy of the beam and the ones with the harmonic energy since they are well separated. A distribution of p_{\max} values for a sensor exposed to a beam also containing photons with harmonic energy is shown on Fig. 11. With the assumption that the tallest distribution corresponds to the voltage values of peaks induced by photons with the base energy of the beam, the p_{\max} values associated with the harmonic energy should lay around twice that of the main peak. In the distribution shown as an example, the base energy corresponds to the distribution around 131 mV and the harmonic one around 248 mV. With this selection, it's possible to extend the energy resolution measurements to twice the range in beam energy.

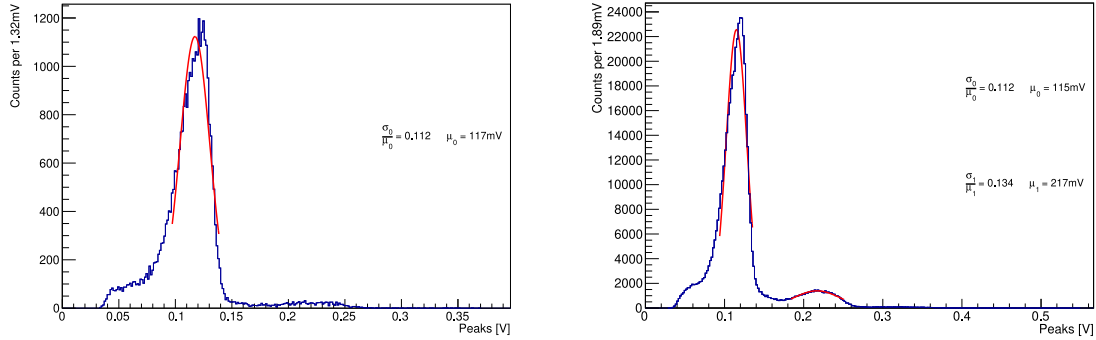


Figure 11: Left: p_{\max} distribution for a HPK Type3.1 LGAD sensor biased at 200 V exposed to a beam of 30 keV X-rays. Right: the same setup when exposed to a beam also containing the 60 keV harmonics shows a second distribution around double the p_{\max} value, this distribution is used to extract the energy and time resolution for the harmonic energies.

6.4 Energy resolution

To extract the energy resolution of a sensor, a histogram is filled with all p_{\max} pertaining to signals induced by X-rays with same energy and the ratio $\frac{\sigma}{\mu}$ of the fit of the p_{\max} distribution is then calculated. In this work, this ratio is presented as the energy estimation resolution of the sensor.

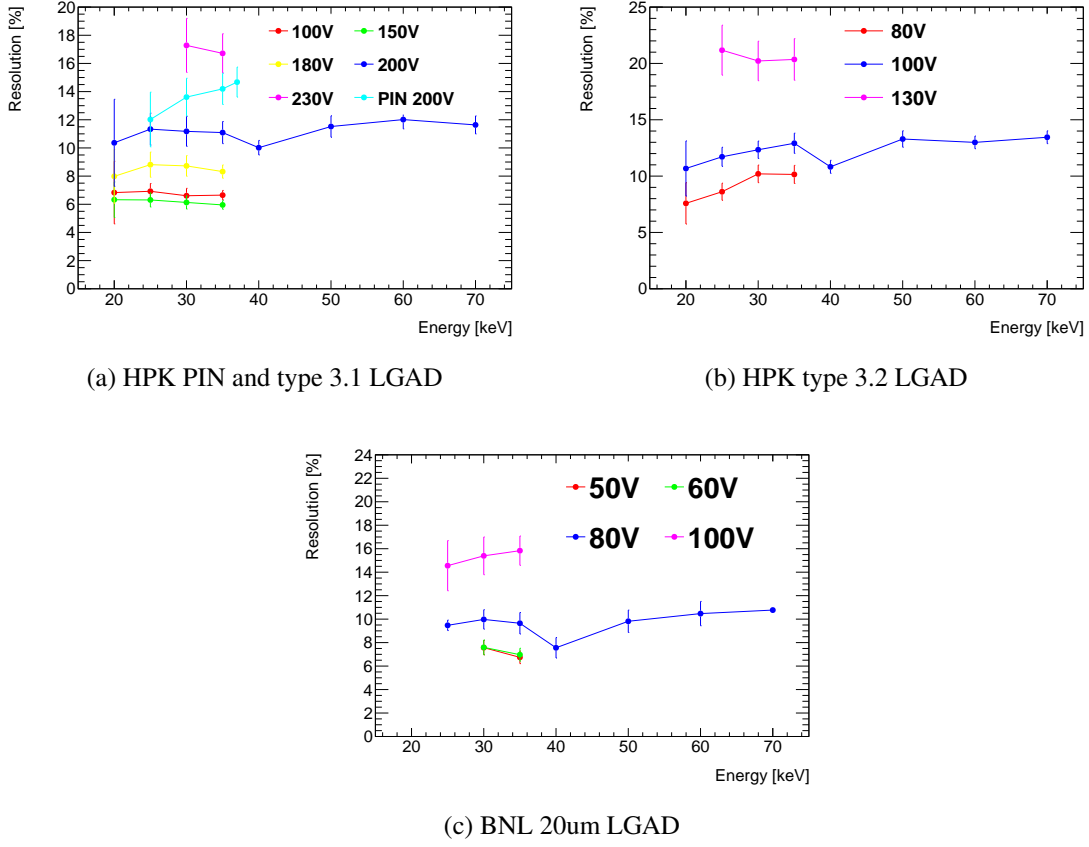


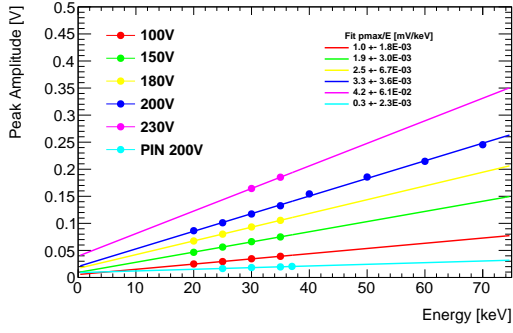
Figure 12: Energy resolution as $\frac{\sigma}{\mu}$ for the different bias voltages used on this test.

In Fig. 11, an example histogram filled with all p_{\max} satisfying the criteria explained in 6.2 for a HPK Type 3.1 LGAD sensor biased at 100 V exposed to a beam of 35 keV X-rays is shown. The distribution of p_{\max} related to the base energy can be seen as the tallest peak corresponding to approximately 39 mV.

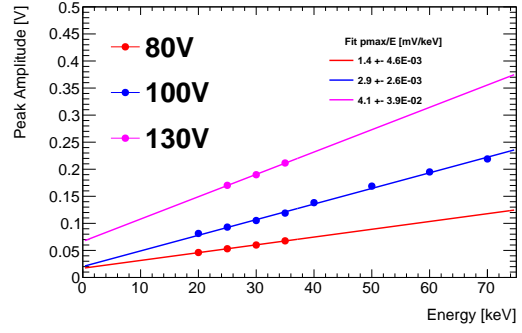
The estimated energy resolution is shown in Fig. 12 for the three sensors tested as a function of energy for different biasing voltages for various X-ray beam energies including harmonics energies. Resolution is shown as the ratio between the standard deviation and the mean of a Gaussian function fit of the tallest peak in the distribution ($\frac{\sigma}{\mu}$) in % for baseline energies. Energies above that of 35 keV are from harmonics, and the Gaussian fit on the distribution in this case is between double the range of values of the tallest peak. The energy resolution measured is below 10% for most devices and voltages. It can be seen that when LGADs are operated with high gain the energy resolution deteriorates.

6.5 Energy calibration and linearity

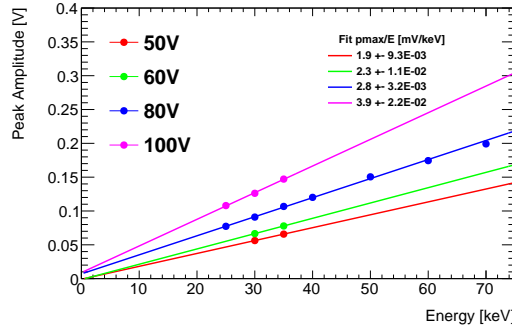
The average of the p_{\max} distribution Gaussian fit described in the previous is taken as the estimation of the energy response of the sensor for the given X-ray energy. In Fig. 13 the relations between energy and the p_{\max} average are shown and a linear fit for the data of the same biasing voltage is performed. The tested sensors show a linear response to X-ray energy at all tested bias voltages.



(a) HPK PIN and type 3.1 LGAD



(b) HPK type 3.2 LGAD



(c) BNL 20um LGAD

Figure 13: Energy response of the 3 sensors tested.

6.6 Time resolution

The timing signal of the cyclotron is used as time reference for the timing resolution measurement of the sensors. To each valid pulse meeting the criteria on 6.2, the time marking of a constant fraction discrimination processing (CFD) at 0.2 fraction modulus 2.1 ns fills a histogram showing the deviation from a constant phase. In Fig. 14, an example of such distribution is shown for an HPK Type 3.1 LGAD sensor biased at 230 V exposed to a beam of 35 keV. In Fig. 14, the timing resolution estimation using a CFD at 20 % fraction is shown for the three sensors measured in this test for different biasing voltages and X-ray beam energies. The time resolution measured is mostly a flat distribution between 50 ps and 150 ps for most devices.

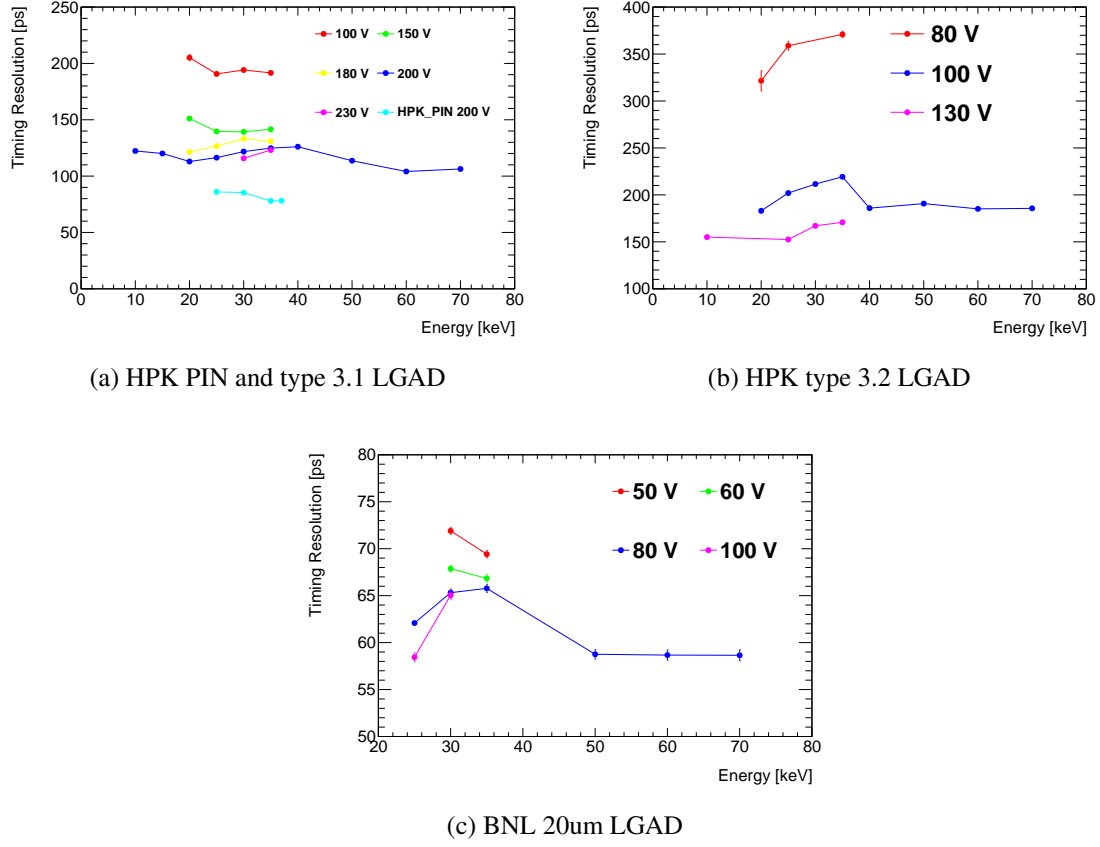


Figure 14: Timing resolution using the repetition rate of the photon source as reference for the sensors tested using a Constant Fraction Discriminator with 20%.

6.7 Results

The best achieved energy and time resolution for the LGAD and PIN geometries tested are shown in Tab. 2. The trade-off between the best energy resolution for a lower bias voltage and the best time resolution for a higher bias can be seen for the 3 LGAD sensors.

	HPK PIN	HPK3.1		HPK3.2		BNL 20um	
Bias V	200V	150V	230V	80V	130V	50V	100V
Energy Res.	14%	6%	17%	10%	20%	6%	16%
Response	19 mV	75 mV	185 mV	68 mV	211 mV	66 mV	147 mV
σ_T CFD	78ps	141ps	123ps	371ps	171ps	69ps	65ps

Table 2: Summary of energy and time resolution for the three tested sensors for the different bias voltages that yields the best energy and best time resolution for a 35 keV X-ray beam energy.

7 Average pulse analysis

The distribution of the pulse maximum and time of the pulse maximum for each event is shown in Fig. 16. The plot is for sensor HPK 3.1 biased at 200V for an X-ray energy of 30 keV. A selection

on P_{\max} of at least 10 mV was applied to remove noise events. The distribution is repeated every 2.1 ns as expected from the SSRL cycle. In the distribution, a few different populations of events are divided as follows. Until 50 mV is a pool of events likely coming from X-rays hitting areas of the sensor with low or no gain (e.g., detector sides or in the region before the gain layer). Between 50 mV and 150 mV is the leading distribution for 30 keV X-rays. The variation in T_{\max} in the main distribution can be explained by the depth of the X-ray absorption inside the detector, as shown in Fig. 8. The events for P_{\max} over 150 mV are for either double photon absorption or from the harmonic component with an energy of 60 keV. It's difficult to separate the two components even though there's a slight gain reduction in the case of the absorption of an X-ray with twice the energy, as seen in Fig. 9.

A slight gain loss is expected when the photon interacts close to the gain layer, as seen in Fig. 8. This can be explained as the effect of the charge density on the electric field, which is reduced, and therefore, the gain is reduced. When the charge is deposited deeper into the detector, the electron lateral drift reduces the charge density in the gain layer. However, the observed direct correlation between T_{\max} and P_{\max} in the main distribution is not easily explained. A possible explanation of the correlation could be that the charge density is affecting more the gain reduction than what is predicted by the simulation. The effect is however also observed at low voltages (with low gain) where the gain reduction from the charge density is less.

In Fig. 15, the average waveforms for slices in P_{\max} are shown. The colors of the waveforms correspond to the lines shown in Fig. 16. The waveforms are both un-normalized, highlighting the P_{\max} trend, and normalized, highlighting the T_{\max} trend. The normalized distribution shows that the pulses with larger P_{\max} have a delayed initial rising edge. The initial (within the first 500 ps) step region of the pulse, predicted in Fig. 8, is observed as a different initial slope in the pulse with the highest delay indicated by the arrow. However, because of the large gain and the averaging, the effect is barely visible.

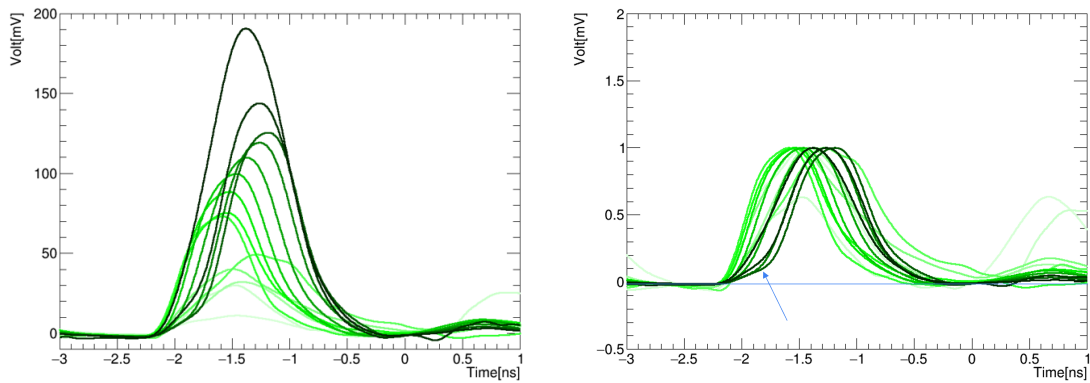


Figure 15: Left: averaged pulses for a subselection of the t_{\max}/p_{\max} plot in Fig. 16. The line color in the pulses and the selection lines in the P_{\max}/T_{\max} plot correspond. Right: same pulses but normalized. The baseline is highlighted with a blue line and the delayed pulse rise is highlighted by the blue arrow.

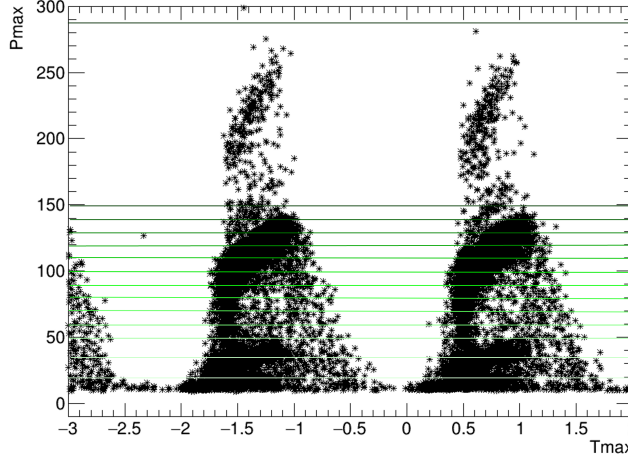


Figure 16: Plot of Pmax (pulse maximum) vs Tmax (time of the pulse maximum) for HPK 3.1 sensor biased at 200V and X-ray energy of 30 keV. Colored lines correspond to sub-selections used to draw the averaged pulse shapes in Fig. 15

8 Energy resolution for AC-LGADs

The energy resolution was also measured for the two AC-LGAD devices in Fig. 17, left. However, the energy response cannot be evaluated using a single-strip readout because of the charge-sharing mechanism [13]. The devices are AC-coupled, so the charge is shared between metal electrodes shown in Fig. 17, right. The data was collected with an IR laser TCT station to emulate the effect of a minimum ionizing particle (MIP). The surface of the device is scanned with a 20 μm laser spot injecting the same energy of a MIP. In the plots, the response of a single strip as a function of the direction perpendicular to the strip is shown. The zero response sections correspond to the metal strips since the metal is not transparent to the laser light. From the laser scans, it can be seen that the charge sharing is mainly limited to the first neighbors for both devices.

The X-ray beam was broad, so no position information was available. This limited the studies that can be performed on AC-LGADs. A simple analysis was applied to measure the energy resolution, although not with the highest precision. A group of three adjacent strips is selected as shown in Fig. 17 (right), and the central strip is required to have the highest signal of the entire sensor. The two neighboring strips need to have a signal lower than the center strip, and the t_{max} is required to be within 600 ps. The p_{max} of the three strips is then summed to measure the deposited energy. The p_{max} distribution of the selected strips is shown in Fig. 18, and the pickup subtracted distribution will be used for measuring the energy resolution. Then, akin to the studies performed in the previous sections, the energy distribution is generated and fitted with a Gaussian to measure central value and resolution. This study was only made with two energies and a low rate (baseline only) to reduce the number of multiple hits on the large sensor. The energy response of the two sensors is linear and with a resolution between 12% and 21%. The 0.5 cm device has a slightly better energy resolution at 37 keV probably related to the lower charge sharing between strips.

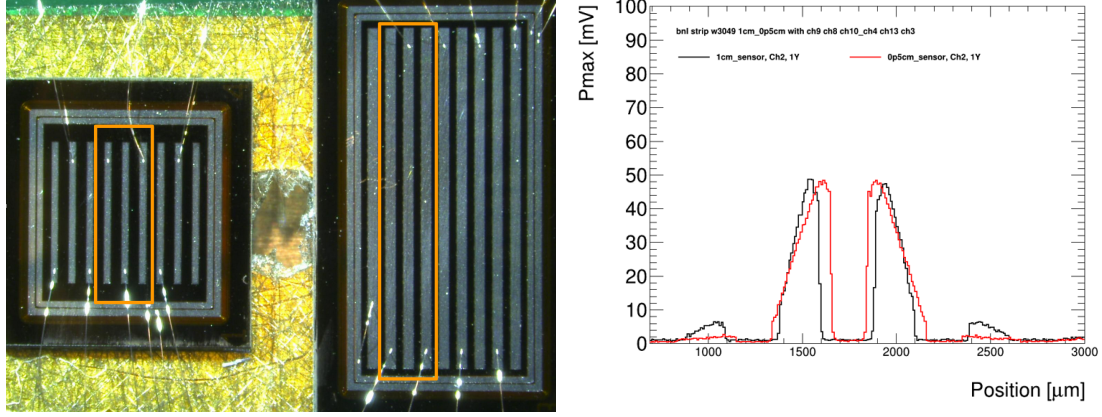


Figure 17: Left: Picture of AC-LGAD with strip length $0.5 \text{ cm} \times 0.5 \text{ cm}$ and $0.5 \text{ cm} \times 1.0 \text{ cm}$. The signal strips (orange) are highlighted. The sum of p_{max} from the three signal strips will be used to measure the energy resolution. Right: Response of a single strip as a function of position perpendicular to the strip, AC-LGAD with strip length $0.5 \text{ cm} \times 1.0 \text{ cm}$ and $0.5 \text{ cm} \times 0.5 \text{ cm}$, data taken with IR laser TCT setup.

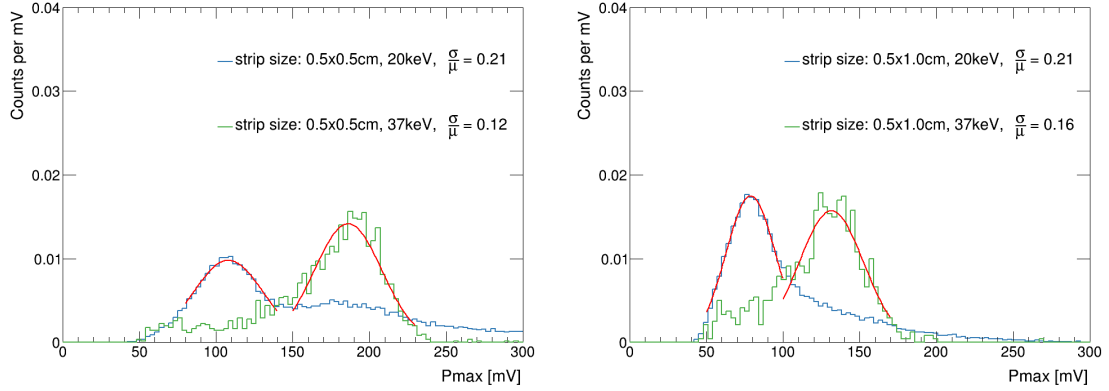


Figure 18: p_{max} distributions for the sum of three selected strips for 0.5 cm long (left) and 1 cm long (right) strip sensors with superimposed energy resolution fit. A selection of 40 mV is applied to the center strip in both cases to remove events not centered in the three strips. The beam was illuminating more the 0.5 cm sensor, this explains the higher tail due to the increased number of double photon events.

9 Conclusions

X-ray detection of silicon devices (LGADs and PiN) was studied at the Stanford Light source (SSRL). The tested thin LGADs easily resolved in time the 500 MHz repetition rate of the beam line. The energy resolution of the tested LGADs was measured to be between 6% and 20%, depending on the X-ray energy and the gain of the device. The best energy resolution (6%) was obtained with LGADs operated at a voltage with a gain of roughly 10. At high voltage the gain fluctuations impact negatively the energy resolution.

The time resolution was estimated to be between 50 ps and 200 ps after time-walk correction, this value is significantly worse than the case of minimum ionizing particles (usually between 20 ps to 50 ps). This is explained by the different charge deposit profiles between minimum ionizing particles and X-rays (point-like); the effect was simulated using TCAD Sentaurus. The time delay due to charge deposition depth was also observed in data using binned averaged waveforms, although with a higher gain variation than the one predicted in the simulation. For each device, the best time resolution is achieved at the maximum voltage. As expected the best time resolution is achieved using the 20 μm device, where the drift time is shorter.

An initial estimation of the energy response of AC-LGADs was made, and it showed an energy resolution of 12-26%, somewhat higher than the DC-LGAD counterpart. However, the broad beam didn't allow for precision studies as a function of position. Energy resolution degradation is expected from the AC nature of the device and the charge-sharing mechanism.

Acknowledgments

This work was supported by the United States Department of Energy, grant DE-FG02-04ER41286. CACTUS DJ-LGAD SBIR

Use of the Stanford Synchrotron Radiation Lightsource, SLAC National Accelerator Laboratory, is supported by the U.S. Department of Energy, Office of Science, Office of Basic Energy Sciences under Contract No. DE-AC02-76SF00515.

The group from USP acknowledges support from FAPESP (grant 2020/04867-2) and CAPES.

References

- [1] ATLAS collaboration, HGTD, *Technical Design Report: A High-Granularity Timing Detector for the ATLAS Phase-II Upgrade*, Tech. Rep. CERN-LHCC-2020-007. ATLAS-TDR-031, CERN, Geneva, Jun, 2020.
- [2] CMS collaboration, *A MIP Timing Detector for the CMS Phase-2 Upgrade*, Tech. Rep. CERN-LHCC-2019-003. CMS-TDR-020, CERN, Geneva, Mar, 2019.
- [3] Z. Galloway, C. Gee, S. Mazza, H. Ohldag, R. Rodriguez, H.-W. Sadrozinski et al., *Use of “lgad” ultra-fast silicon detectors for time-resolved low-keV x-ray science*, *Nuclear Instruments and Methods in Physics Research Section A: Accelerators, Spectrometers, Detectors and Associated Equipment* **923** (2019) 5 – 7.
- [4] G. Pellegrini et al., *Technology developments and first measurements of Low Gain Avalanche Detectors (LGAD) for high energy physics applications*, *Nucl. Instrum. Meth.* **A765** (2014) 12 – 16.
- [5] H. F. W. Sadrozinski et al., *Ultra-fast silicon detectors (UFSD)*, *Nucl. Instrum. Meth.* **A831** (2016) 18–23.
- [6] Stanford Light Source, “<https://www-ssrl.slac.stanford.edu/content/>.”
- [7] SSRL BL 11-2, “<https://www-ssrl.slac.stanford.edu/content/beam-lines/bl11-2>.”
- [8] J. Allison, K. Amako, J. Apostolakis, H. Araujo, P. Arce Dubois, M. Asai et al., *Geant4 developments and applications*, *IEEE Transactions on Nuclear Science* **53** (2006) 270–278.

- [9] J. Allison, K. Amako, J. Apostolakis, P. Arce, M. Asai, T. Aso et al., *Recent developments in geant4*, *Nuclear Instruments and Methods in Physics Research Section A: Accelerators, Spectrometers, Detectors and Associated Equipment* **835** (2016) 186–225.
- [10] S. Agostinelli, J. Allison, K. Amako, J. Apostolakis, H. Araujo, P. Arce et al., *Geant4—a simulation toolkit*, *Nuclear Instruments and Methods in Physics Research Section A: Accelerators, Spectrometers, Detectors and Associated Equipment* **506** (2003) 250–303.
- [11] R. Chytrcek, J. McCormick, W. Pokorski and G. Santin, *Geometry description markup language for physics simulation and analysis applications*, *IEEE Transactions on Nuclear Science* **53** (2006) 2892–2896.
- [12] S.-J. Baek, A. Park, Y.-J. Ahn and J. Choo, *Baseline correction using asymmetrically reweighted penalized least squares smoothing*, *Analyst* **140** (2015) 250–257.
- [13] R. Heller et al., *Characterization of BNL and HPK AC-LGAD sensors with a 120 GeV proton beam*, *JINST* **17** (2022) P05001, [2201.07772].